ACS APPLIED MATERIALS & INTERFACES

Research Article

www.acsami.org

High Efficiency Solar Cells As Fabricated by Sb_2S_3-Modified TiO_2 Nanofibrous Networks

Jian Zhong,[†] Xiaojian Zhang,[†] Yongjia Zheng,[†] Man Zheng,[†] Mingju Wen,[†] Sujuan Wu,*[,†] Jinwei Gao,[†] Xingsen Gao,[†] Jun-Ming Liu,*[,‡] and Hongbo Zhao[§]

[†]Institute for Advanced Materials and [§]School of Physics and Telecommunication Engineering, South China Normal University, Guangzhou 510006, China

[‡]Laboratory of Solid State Microstructures, Nanjing University, Nanjing 210093, China

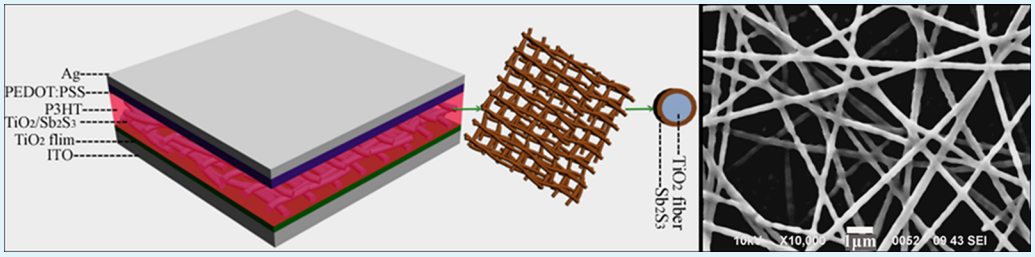

ABSTRACT: High-efficiency hybrid solar cells (HSCs) based on electrospun titanium dioxide (TiO_2) nanofibers plus poly(3-hexylthiophene) (P3HT) are fabricated by means of both the pretreatment using tetrahydrofuran (THF) vapor and the surface modification using n-type antimony chalcogenide (Sb_2S_3) on the TiO_2 nanofibrous networks. It is revealed that the THF pretreatment not only reinforces the interfacial physical contact but also suppresses the interfacial recombination. The Sb_2S_3 modification improves the light absorption and charge transfer. Given that the active layer of the HSCs is as thin as 300 nm, it is demonstrated that the power conversion efficiency (PCE) is enhanced over 175%, exhibiting a PCE of 2.32%.

KEYWORDS: *hybrid solar cells, electrospun TiO_2 nanofibrous networks, THF pretreatment, Sb_2S_3 modification, P3HT*

1. INTRODUCTION

Recently, photovoltaic devices based on composites of n-type inorganic nanomaterials and p-type organic conjugated polymers have attracted much attentions because of their relatively high electron mobility and affinity, high dielectric constant, and potentials for large-area solar cells production at low cost.[1−5] Inorganic nanomaterials also feature high physical and chemical stability. One of the major problems in such kind of hybrid solar cells (HSCs) is the low power conversion efficiency (PCE) because the electron transfer is hindered by both the poor contact at inorganic−organic interface and the broken transport paths in the active layers. A well proven and widely adopted roadmap to improve electron transport both at the interface and in the active layers is to use nanocrystalline structures such as template porous structures,[6] vertically aligned nanorods,[7,8] and electrospun nanofibers.[2−4] Among these options, eletrospinning technique is more promising, as it provides a simple, cost-effective, and large-area approach to prepare various materials with one-dimensional (1D) nanostructures. The as-prepared electrospun nanofibers have already been used in various solar cells. Unfortunately, the efficiency obtained so far is still low (<1.1%) compared with dye-sensitized solar cells.[2]

TiO_2 as an n-type semiconductor is a good candidate for photovoltaic material because of its good air stability, high electron mobility, and appropriate band alignment. So far, the HSCs based on TiO_2 nanostructures yet have low PCE. One reason is that TiO_2 can only absorb the UV region radiation due to its wide band gap. To enhance the light harvesting, we can anchor sensitizers such as organic dye or inorganic semiconductor materials on the surface of TiO_2.[9−11] Inorganic semiconductors offer many advantages such as high extinction coefficient and capability of optical absorption tailoring over a wider wavelength range.[7,8,12−14] Sb_2S_3 as one of metal chalcogenides is an attractive one among these sensitizers. It has high optical absorption coefficient (7.3×10^4 cm^{-1} at 600 nm) and suitable energy band gap of 1.7−1.9 eV. These allow a strong and broad absorption in the visible region, which in turn contributes to more efficient photon harvesting.[7,12,13]

To improve the efficiency of TiO_2 nanomaterial-based HSCs, other aspects include consideration of geometric shapes and material processing. High-surface-area 1D nanofibrous networks can provide large-area interface for charge separation and offer continuous transport paths for photogenerated charges. Moreover, compared with TiO_2/P3HT nanoparticles hybrids, the anisotropic TiO_2 nanofibers in P3HT favor increased vertical stacking of P3HT crystallites, thus providing more effective hole transport perpendicular to the substrate.[15] Another problem associated with P3HT is that oxygen can induce traps in P3HT and deteriorate the performance of

Received: April 8, 2013
Accepted: August 15, 2013
Published: August 15, 2013

   dx.doi.org/10.1021/am401273r | ACS Appl. Mater. Interfaces 2013, 5, 8345−8350

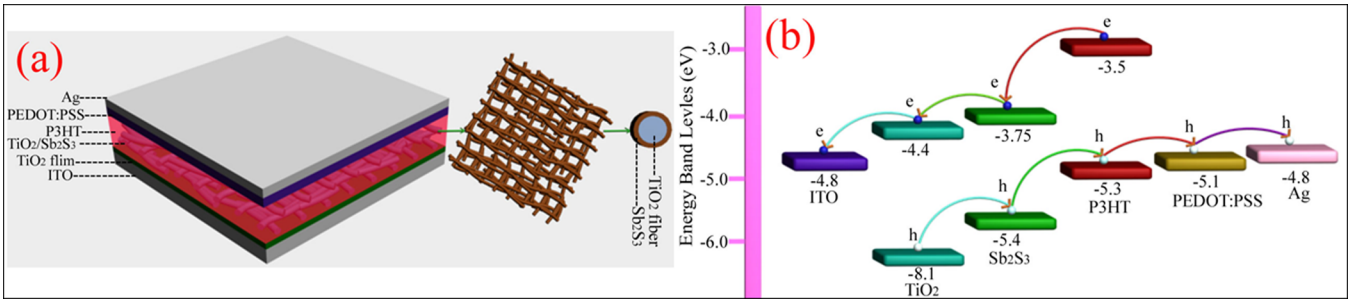

Figure 1. (a) Schematic diagram of the HSC device based on Sb_2S_3-modified TiO_2 nanofibrous networks and P3HT. (b) Corresponding energy level diagram of the corresponding materials used in our devices.

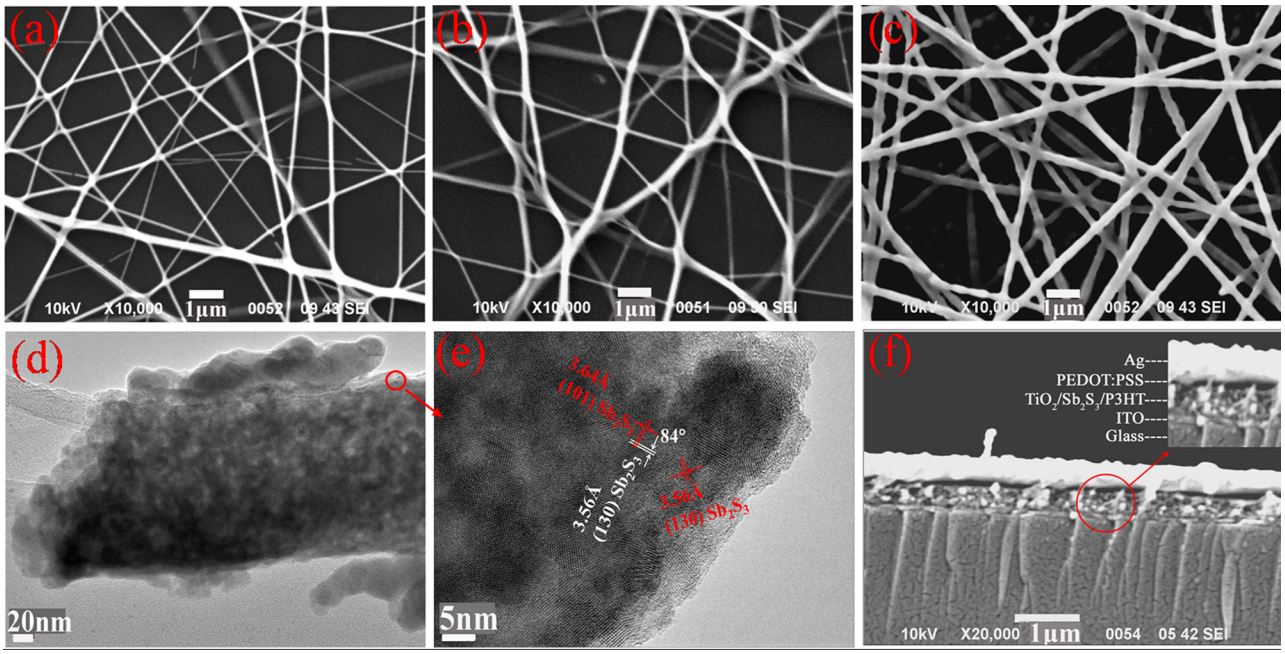

Figure 2. SEM images of (a) TiO_2(UT), (b) TiO_2(T), and (c) TiO_2(T)/Sb_2S_3 nanofibers. (d) TEM image of an electrospun TiO_2 nanofiber modified with Sb_2S_3 (growth time: 3h). (e) High resolution TEM image of Sb_2S_3 deposited on a TiO_2 nanofiber. (f) Cross-sectional SEM view of the TiO_2(T)/Sb_2S_3/P3HT structure. UT, untreated TiO_2 nanofibers; T, TiO_2 nanofibers pretreated with THF vapor.

HSCs.[16−18] Therefore, almost all HSCs based on TiO_2/Sb_2S_3 and P3HT (TiO_2/Sb_2S_3/P3HT) structures are fabricated in inert atmosphere or vacuum. A method that can solve this oxygen-relevant problem and allow device fabrication in air is highly desirable, and will be both cost- and technology-competitive.

Taking care of these considerations, in this work HSCs based on P3HT and electrospun TiO_2 nanofibrous network is fabricated in ambient air. In order to both reinforce the physical contact and increase the interfacial area to facilitate rapid charge separation and transport, we select THF vapor to pretreat the TiO_2 nanofiber networks, then modify the nanofibers by depositing a Sb_2S_3 layer on TiO_2 nanofiber surface. The durations of the THF vapor pretreatment and the Sb_2S_3 layer growth are optimized. Subsequently, we investigate the performance of the HSCs based on the TiO_2/Sb_2S_3/P3HT structures. The recombination in the as-prepared heterojunction is suppressed dramatically upon the THF pretreatment. The light absorption in the visible region is enhanced significantly by Sb_2S_3 modification. Eventually, we demonstrate an improvement of 175% of the PCE with respect to reference cell.

2. EXPERIMENTAL DETAILS

Materials and methods. Figure 1a shows a schematic diagram of the hybrid solar cell (HSC) device to be fabricated in this work. For each sample, cleaned ITO substrate is first coated with a compact TiO_2 film of about 40 nm in thickness by spin-coating sol−gel method. The TiO_2 nanofibrous networks are then electrospun at a flow rate of 0.3 mL/h onto the TiO_2 film surface from a precursor gel containing tetrabutyl titanate (5%) and poly (vinylpyrrolidone) (PVP) (5%) in the solution of isopropanol and 2-methoxyethanol (2:1 in volume) in ambient air. For this electrospinning, a voltage of 9.0 kV between a metal orifice and a grounded rotating collector with a distance of 8 cm is applied for 45 min.

Subsequently, several of the as-prepared samples are chosen as the reference samples and the other samples are submitted to next processing. For the THF vapor pretreatment, the samples are kept for different durations in an anhydrous THF chamber without direct contact with THF. Samples are untreated and chosen as the reference. After the pretreatment, these samples together with the reference samples are annealed at 500 °C for 15 min by rapid thermal processing (RTP) to remove organic components and allow nucleation and growth of TiO_2 grains inside the fibers. Then, the TiO_2 nanofibers besides the reference samples are covered with a Sb_2S_3 layer using a chemical bath deposition method in an aqueous solution of $SbCl_3$ and $Na_2S_2O_3$ in ambient air.[7,19−21] The thickness of the Sb_2S_3 layer is controlled by the growth time.

After the Sb_2S_3 deposition, the as-prepared samples including the reference samples are rinsed thoroughly with deionized water and dried in air, and then annealed in nitrogen (N_2) ambient at 350 °C for 20 min. Here, it is found that the ambient for the subsequent cooling immediately after the annealing is critical for the sample performance. Because the Sb_2S_3 can be partially oxidized to Sb_2O_3 during the cooling process in ambient air and the Sb_2O_3 oxide presumably acts as a passivation layer benefiting to the reduction of the recombination between electrons in the Sb_2S_3 layer and holes in the P3HT.[22] That is why better performance is achieved with the samples cooled in air rather than in N_2.

To fabricate the HSCs stemming from the above samples, a P3HT layer is infiltrated into the TiO_2 nanofibrous networks by spin-coating a solution of P3HT (Reike, regioregularity is ~93%, 20 mg/mL dissolved in toluene) at 1500 rpm for 30 s in ambient air. Our earlier results show that the deposition of P3HT in ambient air can obtain a performance comparable to that of the cells fabricated in an inert environment.[23] So the deposition of P3HT is carried out in ambient air. Subsequently, a layer of poly (3,4-ethylenedioxythiophene):poly (4-styrene sulfonate) (PEDOT:PSS, Bayron P, Bayer A.G.) is spun on the top of P3HT layer in ambient air, followed by thermal annealing at 120 °C for 20 min in a glovebox filled with high purity N_2. Finally, an Ag electrode is evaporated on the sample surface through a shadow mask under a vacuum of 1×10^{-4} Pa and these samples are postannealed at 100 °C for 20 min. To this stage, the HSCs are fabricated with the standard in-plane size of 2 mm × 2 mm. The morphology, dimensions, and crystallinity of the TiO_2 nanofibers covered with the Sb_2S_3 layer are characterized by scanning electron microscopy (SEM, JEOL 5700, Japan), transmission electron microscopy (TEM, F2010, Japan), and X-ray diffraction (XRD, X'Pert PRO, Cu Ká radiation), respectively.

Device Characterizations. The photovoltaic performance of these HSCs is characterized using a Keithley 2400 source meter under an illumination of 100 mW cm^{-2} (Newport 91160, 150W solar simulator equipped with an AM1.5G filter). The radiation intensity is calibrated by a standard silicon solar cell (certified by NREL) as the reference. The external quantum efficiency (EQE) and the UV–vis absorption spectra are measured using a standard EQE system (Newport 66902). The electrochemical impedance spectroscopy (EIS) measurements are performed on the Zahner Zenuium electrochemical workstation in the dark. A 10 mV ac sinusoidal signal source is employed over the constant bias with the frequency ranging from 1 Hz to 4 MHz.

3. RESULTS AND DISCUSSION

The energy level diagram of the TiO_2/Sb_2S_3/P3HT structure is shown in Figure 1b, where the energy levels across the TiO_2, Sb_2S_3, and P3HT are aligned so that the excitation dissociation and charge transfer at the interfaces are energetically favorable. Moreover, successful sensitization of TiO_2 by Sb_2S_3 has been demonstrated, indicating also that the energy levels of Sb_2S_3 and TiO_2 match with each other.[7,12,13,19−21] Figure 2a–c show the SEM images of the only calcined TiO_2 nanofibers (untreated, TiO_2(UT)), TiO_2 nanofibers pretreated with THF vapor (TiO_2(T)), and TiO_2 nanofibers pretreated with THF vapor and modified with Sb_2S_3 (i.e., covered with a Sb_2S_3 layer) (TiO_2(T)/Sb_2S_3), respectively. All these TiO_2 nanofibers for SEM observations are coated on the underlying TiO_2 films, respectively. It is seen that these nanofibers have a diameter distribution over 100–200 nm and they cross over one and another. Such fiber crossing can improve the effective interfacial contact, benefiting to the charge transfer. The THF pretreatment (Figure 2b) induces etched features on the TiO_2 fiber surface, benefiting to the interjunction points and electrical contact between the ITO substrate and TiO_2 fibrous networks.[5]

In comparison with the TiO_2(UT), TiO_2(T)/Sb_2S_3 fibers shown in Figure 2c become much coarser and indicate good interfacial contact between them. And the interpore distance between nanofibrous channels is retained, preserving the effective surface area for P3HT penetration. Figure 2f exhibits the cross-sectional view of the TiO_2(T)/Sb_2S_3/P3HT structure, and it is seen that the space in-between the TiO_2/Sb_2S_3 nanofibers is completely filled with P3HT. The thickness of the TiO_2(T)/Sb_2S_3/P3HT active layer is ~300 nm. Figure 2d, e show the TEM images of a TiO_2/Sb_2S_3 nanofiber at different resolutions. It can be seen that the Sb_2S_3 nanoparticles on the TiO_2 surface have a broad size distribution, and are well-crystallized with lattice constant c of 3.64 Å, consistent with earlier reports.[24] Figure 3a shows the XRD patterns of a dark-brown Sb_2S_3 layer on a slide glass substrate and the prepared condition is identical to that for the Sb_2S_3 layer in the TiO_2(T)/Sb_2S_3/P3HT structure. We can see that the peaks can be well indexed by the stibnite crystal structure (JCPDS 042–1393). Figure 3b shows the energy dispersive X-ray spectrum of a TiO_2/Sb_2S_3 nanofiber, indicating that the fiber contains elements Ti, O, Sb, and S.

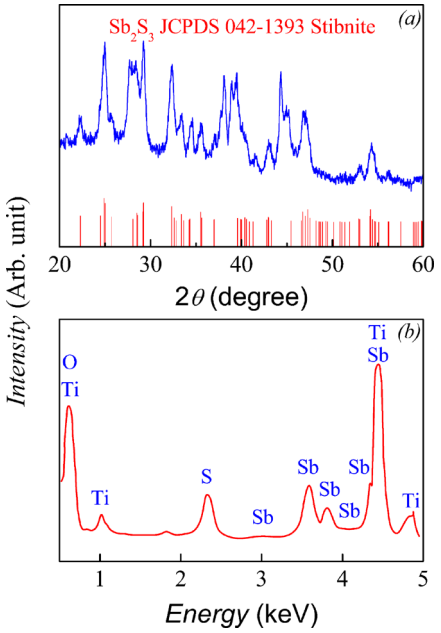

Figure 3. (a) XRD spectrum for Sb_2S_3 thin film deposited on glass substrate in chemical bath for 3h and then annealed at 350 °C for 20 min in N_2 atmosphere. The vertical lines are the characteristic XRD peaks of stibnite crystal structure (JCPDS 042–1393). (b) Energy-dispersive X-ray spectrum of the TiO_2(T)/Sb_2S_3 nanofibers.

It is understood that the thickness of the Sb_2S_3 layer on the TiO_2 nanofiber surface is crucial for the device performance, and it should be optimized to keep a balance between optical absorbance and charge transfer. Figure 4a shows the current density–voltage (J–V) characteristics of a series of TiO_2(UT)/Sb_2S_3/P3HT structures with different Sb_2S_3 growth time. Figure 4b, c show the detailed photovoltaic parameters including the short-circuit current density (J_{sc}), open-circuit voltage (V_{oc}), fill factor (FF) and PCE as functions of the growth time. In the initial stage, J_{sc}, V_{oc}, and PCE all increase with the time, while FF decreases. The reduced FF may be due to the rough nature of the Sb_2S_3 surface, caused by small crystallites developed during the annealing process, leading to small shunt resistance.[8] The duration time for the optimized parameters J_{sc} ~ 9.9 mA/cm^2, V_{oc} ~ 0.591 V, FF ~ 0.33, and

dx.doi.org/10.1021/am401273r | ACS Appl. Mater. Interfaces 2013, 5, 8345–8350

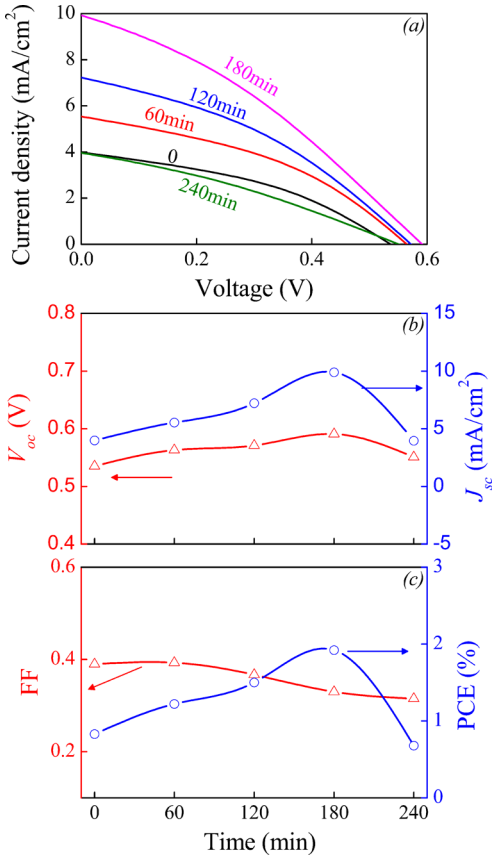

Figure 4. (a) Current−voltage (J−V) curves of TiO_2 (UT)/Sb_2S_3/P3HT structure with different growth times for Sb_2S_3 layer. (b) Measured V_{oc} and J_{sc}, and (c) FF and PCE as a function of the growth time for Sb_2S_3 layer in the TiO_2 (UT)/Sb_2S_3/P3HT structure.

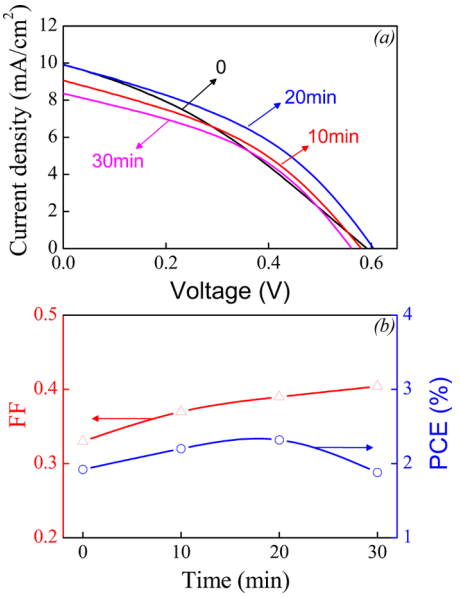

Figure 5. (a) J−V curves, and (b) FF and PCE as a function of THF pretreatment time in the TiO_2(T)/Sb_2S_3/P3HT structure.

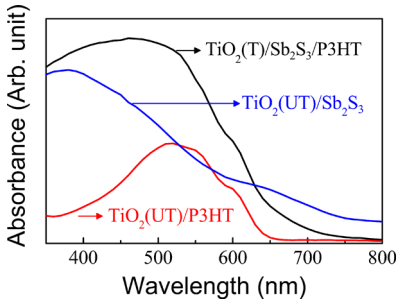

Figure 6. Absorbance spectra of TiO_2(UT)/P3HT, TiO_2(UT)/Sb_2S_3, and TiO_2(T)/Sb_2S_3/P3HT films.

PCE ∼ 1.92%, is 3 h. This optimization can be confirmed by the absorbance spectrum and impedance data to be presented below. The thicker-than-optimal Sb_2S_3 layer yields the lower PCE. This effect is mainly attributed to the decrease in J_{sc} and V_{oc}, because of the difficulty of deep penetration of P3HT, resulting in insufficient charge transport.[12]

The effect of the THF pretreatment on the charge transfer promotion is demonstrated by the J-V curves obtained for different THF duration time, as shown in Figure 5a. Figure 5b demonstrates the dependence of parameters FF and PCE on the time. The PCE increases in the first 20 min and then decreases due to the decay of V_{oc} and J_{sc}. The optimal pretreatment time is 20 min, with the obtained parameters: V_{oc} ∼ 0.603 V, J_{sc} ∼ 9.88 mA/cm^2, FF ∼ 0.39, and PCE ∼ 2.32%.

It is believed that the optimized performance of the HSCs is attributed to three major factors: the increased absorption, accelerated charge transfer due to the interfacial contact reinforcement, and good band alignment at the interface between Sb_2S_3 and P3HT. To clarify this issue, we present in Figure 6 the absorption spectra of the TiO_2(UT)/P3HT, TiO_2(UT)/Sb_2S_3, and TiO_2(T)/Sb_2S_3/P3HT films, respectively. Obviously, the best performance is obtained for the TiO_2(T)/Sb_2S_3/P3HT structure in terms of the high and broad absorption. Because Sb_2S_3 offers high absorption coefficient and proper band gap of 1.7−1.9 eV,[13] the significant increase of the absorption benefits to the increase of J_{sc} due to the Sb_2S_3 coverage and THF vapor pretreatment.

Figure 7a shows the J−V curves for the TiO_2(UT)/P3HT and TiO_2(T)/Sb_2S_3/P3HT structures prepared under the optimal conditions. For the fresh TiO_2(UT)/P3HT structure, one obtains V_{oc} ∼ 0.535 V, J_{sc} ∼ 3.98 mA/cm^2, FF ∼ 0.39, and PCE ∼ 0.83%. The Sb_2S_3 coverage and THF pretreatment allow enhancement of the four parameters up to 0.603 V, 9.88 mA/cm^2, 0.39, and 2.32%, respectively. This implies an improvement of PCE over 175% compared with the fresh structure. Figure 7b presents the measured EQE data for the TiO_2(UT)/P3HT and TiO_2(T)/Sb_2S_3/P3HT structures, indicating the dramatic enhancement in the visible range. The EQE spectrum is consistent with the absorption enhancement induced by the Sb_2S_3. The high EQE in the TiO_2(T)/Sb_2S_3/P3HT structure suggests that our device architecture performs well because of the good band alignment and an intimate contact between the Sb_2S_3 and P3HT, as seen in the cross-sectional SEM of Figure2(f).

For a better understanding of the microscopic mechanisms for the observed enhancement in the performance upon the THF pretreatment and Sb_2S_3 coverage, the EIS and dark J−V measurements are carried out. The EIS is used to evaluate the charge transfer and recombination at the interfaces. In our measurement, two semicircles in the Nyquist plots for each device are observed. As an example, Figure 8(a) shows the Nyquist plots of the EIS data for the TiO_2(T)/Sb_2S_3/P3HT

dx.doi.org/10.1021/am401273r | ACS Appl. Mater. Interfaces 2013, 5, 8345−8350

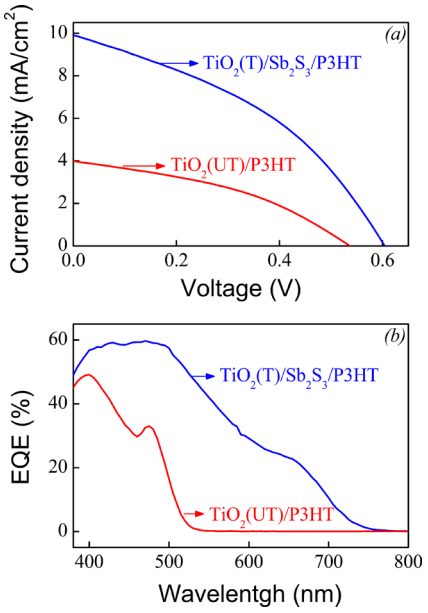

Figure 7. (a) J–V curves, and (b) External quantum efficiency (EQE) of TiO_2(UT)/P3HT and TiO_2(T)/Sb_2S_3/P3HT structures.

structure as a function of bias voltage. The plot shows two major features: one in the high frequency range and the other in the low frequency range. The arc observed in the high frequency range is independent of the applied bias, implying that it does not depend on the Fermi level position and can be ascribed to the parallel association of the capacitance CPE_{ct} of the cells and the charge transfer resistance R_{ct} at the P3HT/PEDOT:PSS/Ag interface.[19] It is noted that this resistance is expected to vary very slowly with voltage. The second is the large semicircle in the low frequency range which is ascribed to the parallel combination of the recombination resistance R_{rec} of electrons in the TiO_2 with that of holes in P3HT or accepting states in Sb_2S_3, and the chemical capacitance CPE_{rec} of electrons in TiO_2.[20] The chemical capacitance is related to the electron Fermi level in TiO_2 caused by the variation of the electron density as a function of bias voltage.[25] The size of the arc in the low-frequency range decreases as the applied bias voltage increases, as shown in Figure 8a. This is due to the decrease in R_{rec} with the increase of electron density. Subsequently, we compare the Nyquist plots for the four structures: TiO_2(UT)/P3HT, TiO_2(UT)/Sb_2S_3/P3HT, TiO_2(T)/Sb_2S_3/P3HT and TiO_2(T)/P3HT at fixed bias voltage of −0.6 V (close to V_{oc}) and the results are presented in Figure 8b. The solid lines in panels a and b in Figure 8 are the fittings of the experimental data using the model in Figure 8c. For more accurate fitting, CPE is used instead of ideal capacitances, C. It can be seen that the measured Nyquist plots can be fitted well. As shown in Figure 8b, compared with the fresh TiO_2(UT)/P3HT structure, the TiO_2(T)/P3HT structure has the highest R_{rec}, whereas the TiO_2(UT)/Sb_2S_3/P3HT shows the lowest R_{rec}.[26−30] This indicates that the recombination rate increases upon the Sb_2S_3 coating, and decreases upon the THF pretreatment because the recombination rate is inversely proportional to R_{rec}.[25] Because the effect of THF pretreatment on the recombination rate is greater than that of Sb_2S_3 coating, the TiO_2(T)/Sb_2S_3/P3HT structure has lower recombination rate than that of TiO_2(UT)/P3HT structure. Although the Sb_2S_3 coating enhances the recombination rate, it significantly increases the light absorption, leading to the

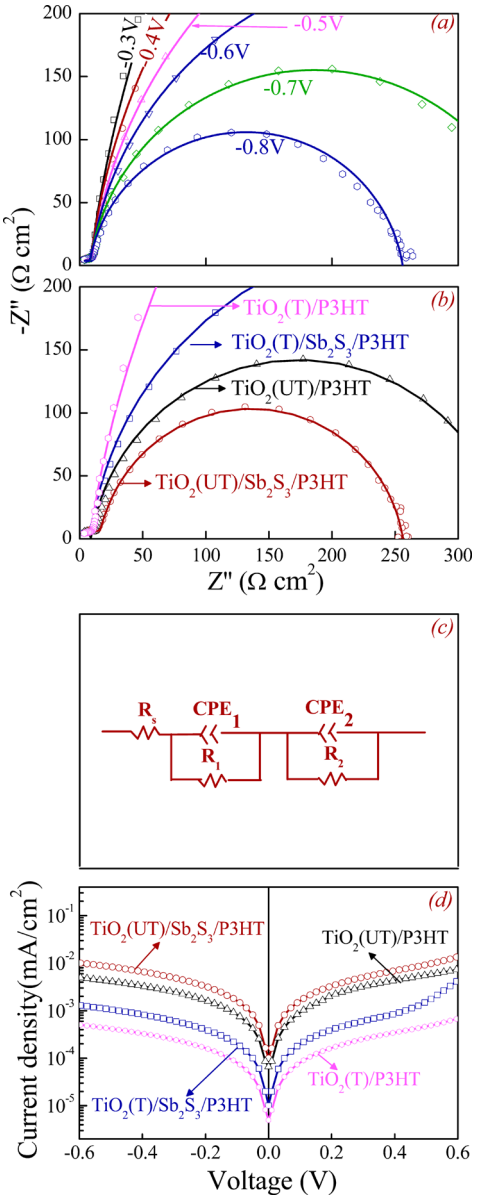

Figure 8. (Color online) (a) Example of Nyquist plots of TiO_2(T)/Sb_2S_3/P3HT structure as a function of bias voltages in the dark. (b) Nyquist plots of TiO_2(UT)/P3HT, TiO_2(UT)/Sb_2S_3/P3HT, TiO_2(T)/Sb_2S_3/P3HT and TiO_2(T)/P3HT structures measured at the bias voltage of −0.6 V (close to V_{oc}) in the dark. (c) Simplified equivalent circuit employed to fit the Nyquist plots. Solid lines in (a) and (b) are the fittings of the experimental data using the model in panel (c). (d) Dark J-V curves of TiO_2(UT)/P3HT, TiO_2(UT)/Sb_2S_3/P3HT, TiO_2(T)/Sb_2S_3/P3HT and TiO_2(T)/P3HT structures.

enhancement of J_{sc}. And the THF pretreatment improves the interjunction and the electrical contact between the ITO substrate and TiO_2 fibrous networks, which will benefit to the effective interfacial contact and charge transfer. Therefore, the TiO_2(T)/Sb_2S_3/P3HT structure shows the best performance. Compared with the TiO_2(UT)/P3HT structure, the better performance in the TiO_2(UT)/Sb_2S_3/P3HT structure can be attributed to the intimate contact between the Sb_2S_3 and P3HT, high and broad light absorption, and the proper band alignment at the interface.[12] Figure 8c shows the equivalent circuit, where a series resistance (R_s) is included because of the contacts and wires.

dx.doi.org/10.1021/am401273r | ACS Appl. Mater. Interfaces 2013, 5, 8345−8350

For further investigation, the dark $J-V$ measurements are conducted for these samples too. Figure 8(d) shows the dark $J-V$ curves of the TiO_2(UT)/P3HT, TiO_2(UT)/Sb_2S_3/P3HT,TiO_2(T)/Sb_2S_3/P3HT and TiO_2(T)/P3HT structures . It is known that the dark current primarily results from the recombination and electron leakage current at the interface of the heterojunctions.[31] Compared with the fresh TiO_2(UT)/P3HT structure, the dark current density in the TiO_2(UT)/Sb_2S_3/P3HT structure is higher, but in the TiO_2(T)/Sb_2S_3/P3HT and TiO_2(T)/P3HT structures they are lower upon the forward bias. For the reverse bias, the TiO_2(UT)/Sb_2S_3/P3HT structure exhibits a higher leakage current compared to the TiO_2(UT)/P3HT structure, suggesting that more recombination events occur because of the presence of the Sb_2S_3 layer. The TiO_2(T)/P3HT structure exhibits the lowest leakage current, indicating that less recombination events occur because of the THF pretreatment. In addition, the lower dark current density in the forward bias indicates less recombination sites and interfacial traps in the TiO_2(T)/Sb_2S_3/P3HT structure. These results allow a conclusion that the TiO_2(T)/Sb_2S_3/P3HT structure not only exhibits efficient light harvesting but also lower recombination rate and thus the best PCE.

4. CONCLUSION

A series of HSCs based on electrospun TiO_2 nanofibrous network and P3HT have been fabricated. We have demonstrated that the THF vapor pretreatment and Sb_2S_3 modification of the TiO_2 nanofibrous networks can improve significantly the performance of the as-prepared HSC. The underlying mechanism is intrinsically related to the increased light absorption and reduced recombination rate at the organic/inorganic heterojunctions. The measured PCE value of the as-prepared HSCs reaches up to 2.32 from 0.83% for the reference HSC without the THF pretreatment and Sb_2S_3 modification.

AUTHOR INFORMATION

Corresponding Authors

*E-mail: sujwu@scnu.edu.cn.
*E-mail: liujm@nju.edu.cn.

Notes

The authors declare no competing financial interest.

ACKNOWLEDGMENTS

We acknowledge the financial support of the National Natural Science Foundation of China (Grant 51003035), Program for Pearl River Star (Grant No. 2012J2200030) and Changjiang Scholars and Innovative Research Team in University (PCSIR).

REFERENCES

(1) Huynh, W. U.; Dittmer, J. J.; Alivisatos, A. P. *Science* **2002**, *295*, 2425−2427.
(2) Tai, Q. D.; Yan, F.; Zhao, X. Z. *J. Mater. Chem.* **2010**, *20*, 7366−7371.
(3) Wu, S. J.; Tai, Q. D.; Yan, F. *J. Phys. Chem. C* **2010**, *114*, 6197−6200.
(4) Wu, S. J.; Li, J. H.; Lo, S. C.; Tai, Q. D.; Yan, F. *Org. Electron* **2012**, *13*, 1569−1575.
(5) Sudhagar, P.; Gonzalez-Pedro, V.; Mora-Sero, I.; Fabregat-Santiago, F.; Bisquert, J.; Kang, Y. S. *J. Mater. Chem.* **2012**, *22*, 14228−14235.
(6) Goh, C.; Coakley, K. M.; McGhee, M. D. *Nano Lett.* **2005**, *5*, 1545−1549.
(7) Cardoso, J. C.; Grimes, C. A.; Feng, X. J.; Zhang, X. Y.; Komarneni, S.; Zanonid, M. V. B.; Bao, N. Z. *Chem. Commun.* **2012**, *48*, 2818−2820.
(8) Coakley, K. M.; Liu, Y. X.; Goh, C.; McGehee, M. D. *MRS Bull.* **2005**, *30*, 37−40.
(9) Lee, Y. L.; Lo, Y. S. *Adv. Funct. Mater.* **2009**, *19*, 604−609.
(10) Kamat, P. V. *Acc. Chem. Res.* **2012**, *45*, 1906−1915.
(11) Lee, H. J.; Chen, P.; Moon, S. J.; Sauvage, F.; Sivula, K.; Bessho, T.; Gamelin, D. R.; Comte, P.; Zakeeruddin, S. M.; Seok, S. I.; Gratzel, M.; Nazeeruddin, M. K. *Langmuir* **2009**, *25*, 7602−7608.
(12) Chang, J. A.; Rhee, J. H.; Im, S. H.; Lee, Y. H.; Kim, H. J.; Seok, S. I.; Nazeeruddin, M. K.; Gratzel, M. *Nano Lett.* **2010**, *10*, 2609−2612.
(13) Im, S. H.; Lim, C. S.; Chang, J. A.; Lee, Y. H.; Maiti, N.; Kim, H. J.; Nazeeruddin, M. K.; Gratzel, M.; Seok, S. I. *Nano Lett.* **2011**, *11*, 4789−4793.
(14) Zeng, T. W.; Liu, I. S.; Hsu, F. C.; Huang, K. T.; Liao, H. C.; Su, W. F. *Opt. Express* **2010**, *18*, A357−A365.
(15) Lin, C. C.; Ho, P. H.; Huang, C. L.; Du, C. H.; Yu, C. C.; Chen, H. L.; Yeh, Y. C.; Li, S. S.; Lee, C. K.; Pao, C. W.; Chu, C. P.; Chang, M. W.; Chen, C. W. *J. Phys. Chem. C* **2012**, *116*, 25081−25088.
(16) Guerrero, A.; Boix, P. P.; Marchesi, L. F.; Ripolles-Sanchis, T.; Pereira, E. C.; Garcia-Belmonte, G. *Sol. Energy Mater. Sol. Cells* **2012**, *100*, 185−191.
(17) Bauld, R.; Fleury, L. M.; Walsh, M. V.; Fanchini, G. *Appl. Phys. Lett.* **2012**, *101*, 103306.
(18) Schafferhans, J.; Baumann, A.; Wagenpfahl, A.; Deibel, C.; Dyakonov, V. *Org. Electron* **2010**, *11*, 1693−1700.
(19) Boix, P. P.; Lee, Y. H.; Fabregat-Santiago, F.; Im, S. H.; Mora-Sero, I.; Bisquert, J.; Seok, S. I. *ACS Nano* **2012**, *6*, 873−880.
(20) Boix, P. P.; Larramona, G.; Jacob, A.; Delatouche, B.; Mora-Sero, I.; Bisquert, J. *J. Phys. Chem. C* **2012**, *116*, 1579−1587.
(21) Lim, C. S.; Im, S. H.; Rhee, J. H.; Lee, Y. H.; Kim, H. J.; Maiti, N.; Kang, Y. K.; Chang, J. A.; Nazeeruddin, M. K.; Gratzel, M.; Seok, S. I. *J. Mater. Chem.* **2012**, *22*, 1107−1111.
(22) Itzhaik, Y.; Niitsoo, O.; Page, M.; Hodes, G. *J. Phys. Chem. C* **2009**, *113*, 4254−4256.
(23) Wu, S. J.; Li, J. H.; Tai, Q. D.; Yan, F. *J. Phys. Chem. C* **2010**, *114*, 21873−21877.
(24) Hu, H. M.; Mo, M. S.; Yang, B. J.; Zhang, X. J.; Li, Q. W.; Yu, W. C.; Qian, Y. T. *J. Cryst. Growth* **2003**, *258*, 106−112.
(25) Fabregat-Santiago, F.; Garcia-Belmonte, G.; Mora-Sero, I.; Bisquert, J. *Phys. Chem. Chem. Phys.* **2011**, *13*, 9083−9118.
(26) Franceschetti, D. R.; Macdonald, J. R.; Buck, R. P. *J. Electrochem. Soc.* **1991**, *138*, 1368−1371.
(27) Adachi, M.; Sakamoto, M.; Jiu, J.; Ogata, Y.; Isoda, S. *J. Phys. Chem. B* **2006**, *110*, 13872−13880.
(28) Hodes, G. *J. Phys. Chem. C* **2008**, *112*, 17778−17787.
(29) Mora-Sero, I.; Gimenez, S.; Fabregat-Santiago, F.; Gomez, R.; Shen, Q.; Toyoda, T.; Bisquert, J. *Acc. Chem. Res.* **2009**, *42*, 1848−1857.
(30) Mora-Sero, I.; Gimenez, S.; Fabregat-Santiago, F.; Azaceta, E.; Tena-Zaera, R.; Bisquert, J. *Phys. Chem. Chem. Phys.* **2011**, *13*, 7162−7169.
(31) Musselman, K. P.; Marin, A.; Schmidt-Mende, L.; MacManus-Driscoll, J. L. *Adv. Funct. Mater.* **2012**, *22*, 2202−2208.